The Astrophysical Journal, 939:41 (14pp), 2022 November 1 https://doi.org/10.3847/1538-4357/ac96ed

Magellan/IMACS Spectroscopy of Grus I: A Low Metallicity Ultra-faint Dwarf Galaxy*

Anirudh Chiti[1,2], Joshua D. Simon[3], Anna Frebel[4], Andrew B. Pace[5], Alexander P. Ji[1,2], and Ting S. Li[6]
[1] Department of Astronomy & Astrophysics, University of Chicago, 5640 S Ellis Avenue, Chicago, IL 60637, USA; achiti@uchicago.edu
[2] Kavli Institute for Cosmological Physics, University of Chicago, Chicago, IL 60637, USA
[3] Observatories of the Carnegie Institution for Science, 813 Santa Barbara Street, Pasadena, CA 91101, USA
[4] Department of Physics and Kavli Institute for Astrophysics and Space Research, Massachusetts Institute of Technology, Cambridge, MA 02139, USA
[5] McWilliams Center for Cosmology, Carnegie Mellon University, 5000 Forbes Avenue, Pittsburgh, PA 15213, USA
[6] Department of Astronomy and Astrophysics, University of Toronto, 50 St. George Street, Toronto ON, M5S 3H4, Canada
Received 2022 June 9; revised 2022 September 21; accepted 2022 September 22; published 2022 November 2

Abstract

We present a chemodynamical study of the Grus I ultra-faint dwarf galaxy (UFD) from medium-resolution ($R \sim 11{,}000$) Magellan/IMACS spectra of its individual member stars. We identify eight confirmed members of Grus I, based on their low metallicities and coherent radial velocities, and four candidate members for which only velocities are derived. In contrast to previous work, we find that Grus I has a very low mean metallicity of $\langle$[Fe/H]$\rangle = -2.62 \pm 0.11$ dex, making it one of the most metal-poor UFDs. Grus I has a systemic radial velocity of $-143.5 \pm 1.2\,\mathrm{km\,s^{-1}}$ and a velocity dispersion of $\sigma_{\mathrm{rv}} = 2.5^{+1.3}_{-0.8}\,\mathrm{km\,s^{-1}}$, which results in a dynamical mass of $M_{1/2}(r_h) = 8^{+12}_{-4} \times 10^5\ M_\odot$ and a mass-to-light ratio of $M/L_V = 440^{+650}_{-250}\ M_\odot/L_\odot$. Under the assumption of dynamical equilibrium, our analysis confirms that Grus I is a dark-matter-dominated UFD ($M/L > 80\ M_\odot/L_\odot$). However, we do not resolve a metallicity dispersion ($\sigma_{\mathrm{[Fe/H]}} < 0.44$ dex). Our results indicate that Grus I is a fairly typical UFD with parameters that agree with mass–metallicity and metallicity-luminosity trends for faint galaxies. This agreement suggests that Grus I has not lost an especially significant amount of mass from tidal encounters with the Milky Way, in line with its orbital parameters. Intriguingly, Grus I has among the lowest central densities ($\rho_{1/2} \sim 3.5^{+5.7}_{-2.1} \times 10^7\ M_\odot\ \mathrm{kpc^{-3}}$) of the UFDs that are not known to be tidally disrupting. Models of the formation and evolution of UFDs will need to explain the diversity of these central densities, in addition to any diversity in the outer regions of these relic galaxies.

Unified Astronomy Thesaurus concepts: Dwarf galaxies (416); Population II stars (1284)

1. Introduction

Over the last two decades, data from large digital sky surveys (e.g., the Sloan Digital Sky Survey (SDSS), the Dark Energy Survey (DES), and PanSTARRS) have led to an order-of-magnitude increase in the number of known low surface brightness stellar systems in the vicinity (<200 kpc) of the Milky Way (e.g., Willman et al. 2005a, 2005b; Zucker et al. 2006; Belokurov et al. 2007; Walsh et al. 2007; Willman 2010; Koposov et al. 2015a; Laevens et al. 2015a, 2015b; Bechtol et al. 2015; Drlica-Wagner et al. 2015, 2016; Kim & Jerjen 2015; Kim et al. 2015; Homma et al. 2016, 2018; Mau et al. 2020; Cerny et al. 2021, 2022). One particularly intriguing class of faint systems, which were first detected in SDSS data over a decade ago (Willman et al. 2005a, 2005b), are ultra-faint dwarf galaxies (UFDs). UFDs are the least luminous ($L < 10^5\ L_\odot$; Simon 2019), most dark-matter dominated ($\gtrsim$100 $M_\odot/L_\odot$; Simon & Geha 2007), and among the oldest ($\sim$13 Gyr; e.g., Brown et al. 2014) stellar systems. Consequently, they are unique nearby probes of galaxy formation on the smallest scales (e.g., Rey et al. 2019), early chemical evolution (e.g., Frebel et al. 2014), and indirect signatures of dark-matter interactions (e.g., Abdallah et al. 2020).

An initial step in characterizing UFDs is to derive their dynamical masses and metallicities through spectroscopy of member stars. This step is crucial, because it is often ambiguous upon discovery whether a faint system is a bona fide UFD or a globular cluster (GC; Willman & Strader 2012). One distinguishing feature between GCs and UFDs is that GCs are not dark-matter dominated ($M/L \lesssim 3\ M_\odot/L_\odot$; McLaughlin & van der Marel 2005) whereas UFDs are the most dark-matter-dominated known systems ($\gtrsim$100 $M_\odot/L_\odot$; Simon & Geha 2007). From spectroscopy, one can derive the velocity dispersion of member stars, which can then be used to derive a dynamical mass (Walker et al. 2009b; Wolf et al. 2010) and an accompanying mass-to-light ratio for classification. A metallicity dispersion can also be used to separate GCs from UFDs, since UFDs show significant metallicity spreads (e.g., Frebel et al. 2014) whereas GCs show minimal spreads ($\lesssim$0.05 dex; e.g., Carretta et al. 2009). Differences in chemical abundance patterns are also observed (e.g., Ji et al. 2019).

Simply identifying a system as a UFD and presenting its general properties (e.g., dynamical mass, mean metallicity, and dispersion) is of scientific interest. For instance, the number and distribution of the Milky Way's UFDs can constrain models of dark matter (e.g., Kim et al. 2018; Nadler et al. 2021; Mau et al. 2022). Whether a UFD lies on the luminosity−mass relation for dwarf galaxies (Kirby et al. 2013b) can indicate mass loss from interactions with the Milky Way (e.g., Simon et al. 2017; Li et al. 2018a). And the kinematics of stars in a UFD can be used to derive a J factor to determine the relevance of the system for indirect searches for signatures of dark-matter interactions (e.g., Pace & Strigari 2019).

* This paper includes data gathered with the 6.5 m Magellan Telescopes located at Las Campanas Observatory, Chile.

In this regard, Grus I is a particularly interesting Milky Way satellite as its classification has remained somewhat ambiguous. The system was first discovered in DES DR1 data as a metal-poor, faint ($M_V = -3.4 \pm 0.3$) satellite (Koposov et al. 2015a); although, its location near a DECam chip-gap in the DES imaging rendered its structural properties uncertain. Subsequent, wide-field photometric follow-up (Cantu et al. 2021) derived a half-light radius of $r_h = 151^{+21}_{-31}$ pc and a photometric $\langle [Fe/H] \rangle = -1.88^{+0.09}_{-0.03}$, suggesting Grus I to be a UFD due to its large size but with a higher than typical UFD metallicity. Jerjen et al. (2018) found a lower metallicity of $\langle [Fe/H] \rangle = -2.50^{+0.30}_{-0.30}$ in their photometric study of Grus I. An initial spectroscopic study of Grus I by Walker et al. (2016) was unable to resolve a velocity dispersion and derived a mean metallicity of $\langle [Fe/H] \rangle = -1.42^{+0.55}_{-0.42}$ from seven probable member stars. Such a metallicity, at face value, is abnormally high for a UFD (typically $\langle [Fe/H] \rangle < -2.0$; Simon 2019), but the large uncertainty on the metallicity precluded a clear classification.

Recent observations have hinted that Grus I is a UFD. The brightest two stars in Grus I have $[Fe/H] \approx -2.5$ and show deficiencies in neutron-capture element abundances, which is a distinctive signature of UFD stars (Ji et al. 2019). A recent study presented in Zoutendijk et al. (2021) supports the classification of Grus I as a UFD by detecting a large, but uncertain, velocity dispersion of $10.4^{+9.3}_{-5.1}$ km s^{-1} using MUSE data ($R \sim 3000$). However, this study does not derive spectroscopic metallicities for its sample of members, and only selects Grus I member stars through a kinematic selection. This can artificially inflate the derived velocity dispersion by making the sample susceptible to contamination from more metal-rich foreground Milky Way halo stars that have similar kinematics to Grus I. A detailed and uniform study of Grus I, with a joint metallicity and kinematic analysis is therefore needed to conclusively determine its nature.

In this paper, we present a comprehensive study of member stars in Grus I with new spectroscopy from Magellan/IMACS. We reobserve all likely members that were presented in Walker et al. (2016) to derive independent velocity and metallicity measurements, and to search for any binary stars. From our joint metallicity and velocity analysis, we identify eight member stars and derive a mean metallicity of $\langle [Fe/H] \rangle = -2.62 \pm 0.11$ and a velocity dispersion of $\sigma = 2.5^{+1.3}_{-0.8}$ km s^{-1}, confirming that Grus I is a canonical dark-matter-dominated UFD ($M/L_V = 440^{+650}_{-250}$ $M_\odot/L_\odot$ and $M/L_V > 80$ $M_\odot/L_\odot$). We then comment on the orbital history and evolution of Grus I based on its derived properties and our sample of members.

This paper is organized as follows. In Section 2, we describe our observations. In Section 3, we outline our methodology in deriving velocities, metallicities, and identifying members. In Section 4, we derive the dynamical mass, mean metallicity, and orbit of Grus I, and comment on its evolution, and in Section 5, we conclude.

2. Observations and Data Reduction

2.1. Summary of Observations

We observed Grus I using the IMACS spectrograph (Dressler et al. 2006) on the Magellan-Baade Telescope with three separate multi-slit masks in 2015 July, 2019 October, and 2021 September, respectively (see Table 1 for details). We operated the spectrograph following previous multi-slit spectroscopic studies of UFDs using the IMACS instrument (e.g., Li et al. 2017; Simon et al. 2017, 2020), which we briefly outline here. The observations were performed using the f/4 camera, which nominally granted a 15.′4 by 15.′4 field of view for slit placement. We used a slit size of 0.″7 and the 1200 ℓ mm^{-1} grating at a tilt angle of 32.°4, which granted a resolution of $R \approx 11{,}000$ and wavelength range of ∼7500 to ∼9000 Å. This wavelength range is sufficient to cover the prominent telluric *A*-band feature (∼7600 Å) and the calcium triplet absorption lines (8498, 8542, and 8662 Å). This setup grants a minimum velocity precision of ∼1 km s^{-1} (e.g., Simon et al. 2017). We note that the exact wavelength range varies for each spectrum based on the location of the slit on the multi-slit mask. However, we placed slits to ensure that at least the calcium triplet region (8450–8700 Å) was covered for each star.

Our observing sequence included two to three science exposures of 1800–3300 s, followed by an arc frame for wavelength calibration, and then a quartz frame for order-tracing and flat-fielding purposes. We note that we used HeNeAr reference lamps for the wavelength calibration of our observations in 2015, but switched to KrHeNeAr lamps for all subsequent observations in order to make use of strong Kr lines between 7600 and 7900 Å. The weather was mediocre (∼1.″0 seeing) during the 2015 observations, ∼0.″7 seeing with occasional cirrus for the 2019 observations, and ∼0.″6 seeing with clear skies for the 2021 observations. Table 1 lists the details of our observations.

We reduced the data following Simon et al. (2017) and Li et al. (2017). The COSMOS reduction pipeline (Dressler et al. 2011; Oemler et al. 2017) was used to locate the slits on the CCD array, generate an initial wavelength solution, and extract 2D spectra. Then, we used a modified version of the DEEP2 reduction pipeline (Cooper et al. 2012; Newman et al. 2013) that had been altered by Simon et al. (2017) to refine the IMACS wavelength solution and extract 1d spectra.

2.2. Target Selection

We observed Grus I using three multi-slit masks (see Table 1). Targets for Mask 1 were selected by overlaying a 12 Gyr, $[Fe/H] = -2.5$ Dartmouth isochrone (Dotter et al. 2008) at the assumed distance modulus of Grus I ($m - M = 20.4$; Koposov et al. 2015a) on a *g*, *r* color–magnitude diagram of stars within 20.′0 of Grus I. The color–magnitude diagram for this selection was generated by running a default configuration of Source Extractor (Bertin & Arnouts 1996) on DES images of Grus I that were retrieved from the NOAO public data archive (Flaugher et al. 2015; Morganson et al. 2018). We identified stars within 0.1 mag of the isochrone as candidate Grus I members and ultimately selected 28 stars for inclusion on this mask, limited by constraints arising from slit placement.

Mask 2 was designed using photometry from DES DR1 (Abbott et al. 2018). Target selection was carried out with a 12.5 Gyr, $[Fe/H] = -2.3$ Dartmouth isochrone, identifying stars within 0.08 mag of the red giant branch (RGB) and with Gaia DR2 proper motions consistent with that of Gru I. Eleven RGB candidates were included on the mask. Mask 3 was designed to obtain an additional measurement of the two brightest member stars identified from the previous masks, which each exhibited possible signs of weak radial velocity variations.

Table 1
Observations

Mask Name	R.A. (hh:mm:ss) (J2000)	Decl. (dd:mm:ss) (J2000)	Slit PA (deg)	t_{exp} (min)	Date of Observation (YYYY/MM/DD)	MJD of Observation[a]	Number of Slits	Number of Useful Spectra[b]
Mask 1	22:56:40	−50:10:40	90	225	2015/7/26	57229.33	28	17
Mask 2	22:56:36	−50:08:59	214	180	2019/10/6	58762.03	72	61
Mask 3[c]	22:56:53	−50:08:30	72	30	2021/9/14	59471.02	6	3

Notes.
[a] For masks observed over multiple nights, we list the midpoint MJD of observation.
[b] Defined as having a velocity measurement in Table 2.
[c] Mask 3 was designed to obtain additional velocities for previously confirmed, bright Grus I members in Masks 1 and 2.

3. Analysis

3.1. Derivation of Radial Velocities

We derived radial velocities following the methods presented in Simon et al. (2017) and Li et al. (2017), which we briefly outline here. We performed a χ^2 minimization between our observed spectra and a template IMACS spectrum of HD 122563 from 8450−8680 Å to measure radial velocities from the calcium triplet features. The template spectrum of HD 122563 was collected using the same 0.″7 slit size and 1200 ℓ mm^{-1} grating as our Grus I observations. We assumed a velocity of -26.51 km s^{-1} for HD 122563 (Chubak et al. 2012). We derived heliocentric velocity corrections using the `astropy` package (Astropy Collaboration et al. 2013, 2018). Random uncertainties on the radial velocity measurements were derived through Monte Carlo resampling: we added noise to each spectrum based on its signal-to-noise (S/N) value, remeasured the radial velocity, and repeated this process 500 times. We took the standard deviation of the resulting velocity distribution, after clipping 5σ outliers, to be the random velocity uncertainty for each star.

We applied a correction to our radial velocities based on the wavelength of the telluric *A*-band absorption feature at ∼7600 Å to account for slit mis-centering effects. We derived this correction by repeating the same steps as for the radial velocity measurement, but instead performing the χ^2 minimization over the wavelength range of 7550–7700 Å with respect to a template spectrum of the hot, rapidly rotating star HR 4781 (Simon et al. 2017). These corrections were typically $\lesssim$5 km s^{-1} and showed a clear dependence on the location of the slit perpendicular to the dispersion axis of the CCD mosaic. We thereby modeled these corrections by fitting a line to the telluric correction as a function of location along this axis of the CCD mosaic, using only measurements from spectra with S/N > 5 to ensure a high-quality sample. We then used this linear model to calculate the telluric correction for each star, which had the additional benefit of providing a robust correction for stars that had low S/N or no wavelength coverage of the *A*-band region.

We derived a systematic velocity uncertainty of 1.1 km s^{-1} on our velocity measurements, based on repeat observations of stars following the methods presented in, e.g., Simon & Geha (2007). Specifically, we divided our raw data into two subsets, independently reduced each subset, and derived velocities from the 1D spectra following the above techniques. Then, we found that a systematic velocity uncertainty of 1.1 km s^{-1} needed to be added in quadrature to the random velocity uncertainties for consistency among the velocity measurement of the same stars (e.g., as in Simon & Geha 2007; Li et al. 2017; Simon et al. 2017). We computed final velocity uncertainties by adding in quadrature the random velocities uncertainties and the systematic velocity uncertainty. If applicable (i.e., if stars showed no evidence for binarity), velocity measurements were combined across multiple runs by taking a weighted average, where the weights were equal to the inverse squared uncertainty of the velocity measurement.

Our radial velocity measurements are presented in Table 2 and in the lower left panel of Figure 1. We find 13 stars with radial velocities roughly consistent with membership to Grus I (between -150 and -130 km s^{-1}). Of these, nine have metallicity measurements; eight of those have low metallicities ([Fe/H] < −2.0) consistent with UFD membership, and one has a higher metallicity ([Fe/H] > −1.0) that is inconsistent with UFD membership (see Figure 2, and further discussion in Section 3.3).

3.2. Derivation of Metallicities

We derived metallicities by using the well-established relationship between the equivalent widths of the calcium triplet absorption lines, the absolute *V* magnitude, and the stellar metallicity (Carrera et al. 2013). We measured equivalent widths of each calcium triplet line by fitting them with a Gaussian plus Lorentzian profile, following Simon et al. (2017) and Li et al. (2017). The apparent *V* magnitude of each star was derived using Equation (5) in Bechtol et al. (2015) and was converted to an absolute magnitude using a Grus I distance modulus of $m - M = 20.48$ (Cantu et al. 2021).

The random uncertainties in the metallicities were derived following the procedure in Simon et al. (2020), in which the statistical uncertainty in the equivalent width from the Gaussian + Lorentzian fit to each line was propagated to derive a metallicity uncertainty. An additional systematic uncertainty of 0.32 Å was added in quadrature to the equivalent width uncertainties (e.g., Simon et al. 2017). The systematic uncertainty in the final metallicities was assumed to be 0.17 dex, following the stated uncertainty of the metallicity calibration in Carrera et al. (2013). We took the final metallicity uncertainty of each star as the quadrature sum of its random uncertainty and the systematic uncertainty. For stars with spectra over multiple epochs, we combined metallicity measurements from the individual spectra by taking the weighted average of the metallicities, where the weights were the inverse square of the metallicity uncertainties.

We note that the calibration we employ is only valid for RGBs that are at the distance of Grus I, since the absolute *V* magnitudes inputted into the calibration are computed assuming the distance modulus of Grus I. We see an artifact of this assumption in Figure 2, where a number of nonmembers of Grus I (e.g., stars with radial velocities inconsistent with membership) have spuriously low metallicities. Accordingly,

Table 2
Velocity Measurements for all Stars

ID	MJD[a]	R.A. (deg)	Decl. (deg)	g[b] (mag)	r[b] (mag)	S/N	v (km s^{-1})	MEM
DES J225619.85-500757.2	58762.03	344.08273	−50.13258	17.4	16.95	64.25	−4.05 ± 1.11	NM
DES J225650.20-500814.2	58762.03	344.20917	−50.13729	21.06	20.57	4.85	−24.18 ± 2.57	NM
DES J225625.52-500828.1	58762.03	344.10635	−50.14116	21.9	20.5	10.77	−5.37 ± 1.65	NM
DES J225613.76-500835.1	58762.03	344.05735	−50.14309	19.57	18.7	23.03	140.71 ± 1.26	NM
DES J225713.21-500834.6	58762.03	344.30507	−50.14297	20.54	19.81	10.85	51.89 ± 1.71	NM
DES J225625.24-500842.0	58762.03	344.10519	−50.14501	20.35	18.87	44.23	46.26 ± 1.14	NM
DES J225631.22-500841.9	58762.03	344.13012	−50.14498	20.04	19.13	20.04	18.57 ± 1.8	NM
DES J225710.06-500856.0	58762.03	344.29192	−50.1489	19.08	18.4	27.45	0.53 ± 1.19	NM
DES J225658.06-501357.9	57229.33	344.24192	−50.23276	18.55	17.49	44.95	−140.88 ± 1.11	M
	58762.03	344.24192	−50.23276	18.55	17.49	53.25	−141.59 ± 1.11	M
	59471.02	344.24192	−50.23276	18.55	17.49	24.79	−143.32 ± 1.13	M
DES J225643.89-500903.0	58762.03	344.18288	−50.15085	21.43	20.93	3.5	−144.37 ± 7.39	CM
DES J225640.97-500913.4	58762.03	344.17074	−50.15374	18.97	18.63	21.8	188.02 ± 1.34	NM
DES J225703.50-500942.6	58762.03	344.26461	−50.16184	22.44	20.91	12.77	21.73 ± 1.92	NM
DES J225720.93-500951.2	58762.03	344.33724	−50.16423	21.2	19.64	30.71	33.11 ± 1.24	NM
DES J225655.34-500947.0	58762.03	344.23059	−50.16308	22.01	20.5	17.49	11.87 ± 1.45	NM
DES J225657.50-501013.9	58762.03	344.23959	−50.17053	20.41	19.06	38.09	62.0 ± 1.15	NM
DES J225710.72-501008.0	58762.03	344.29467	−50.16889	22.37	21.17	3.27	60.63 ± 7.23	NM
DES J225711.61-501018.5	58762.03	344.29838	−50.17182	18.99	19.12	7.75	210.38 ± 6.86	NM
DES J225703.66-501016.2	58762.03	344.26527	−50.17119	19.84	19.52	9.96	84.9 ± 1.79	NM
DES J225632.36-501025.4	58762.03	344.13486	−50.17372	20.0	19.4	10.85	57.61 ± 1.84	NM
DES J225656.51-501044.0	58762.03	344.23547	−50.1789	17.55	17.2	55.85	8.95 ± 1.12	NM
DES J225640.78-501051.4	58762.03	344.16992	−50.18096	20.43	19.79	10.35	−142.49 ± 1.46	M
	59471.02	344.16992	−50.18096	20.43	19.79	5.53	−140.68 ± 2.11	M
DES J225717.17-501105.1	58762.03	344.32157	−50.18477	19.94	19.22	12.78	79.9 ± 1.91	NM
DES J225646.98-501226.9	58762.03	344.19576	−50.2075	21.96	20.78	4.93	12.44 ± 3.69	NM
DES J225657.98-501252.7	58762.03	344.24162	−50.21466	19.18	18.96	15.84	279.45 ± 1.6	NM
DES J225629.92-500433.3	57229.33	344.12467	−50.07593	19.14	18.29	33.67	−147.39 ± 1.15	M
	58762.03	344.12467	−50.07593	19.14	18.29	36.66	−146.38 ± 1.14	M
	59471.02	344.12467	−50.07593	19.14	18.29	15.4	−144.72 ± 1.26	M
DES J225642.47-500334.1	57229.33	344.17699	−50.05949	21.58	21.06	2.02	21.47 ± 10.46	NM
DES J225639.47-500401.0	57229.33	344.16449	−50.06697	18.82	17.91	35.41	13.55 ± 1.16	NM
DES J225619.67-500913.1	57229.33	344.08198	−50.15364	20.9	20.34	6.93	−146.35 ± 2.39	M
	58762.03	344.08198	−50.15364	20.9	20.34	6.34	−139.67 ± 2.24	M
DES J225643.20-501130.0	57229.33	344.18001	−50.19168	21.13	20.48	3.69	−138.53 ± 6.06	NM
	58762.03	344.18001	−50.19168	21.13	20.48	5.26	−138.77 ± 2.31	NM
DES J225643.79-501332.6	57229.33	344.18246	−50.22574	21.51	20.95	2.57	−139.07 ± 6.87	CM
DES J225637.05-501024.8	57229.33	344.15438	−50.17357	20.46	19.81	9.29	−135.25 ± 2.13	M
	58762.03	344.15438	−50.17357	20.46	19.81	9.81	−143.08 ± 1.58	M
DES J225625.69-501414.2	57229.33	344.10707	−50.23729	20.95	20.42	4.35	−144.56 ± 4.0	CM
DES J225653.36-500924.3	57229.33	344.22233	−50.15675	19.9	19.29	13.42	−53.12 ± 1.49	NM
DES J225657.61-500938.5	57229.33	344.24005	−50.1607	19.21	18.43	23.37	54.94 ± 1.29	NM
	58762.03	344.24005	−50.1607	19.21	18.43	29.87	54.98 ± 1.2	NM
DES J225658.78-500832.5	57229.33	344.24495	−50.14237	20.72	20.09	5.15	166.9 ± 2.45	NM
DES J225704.98-501229.6	58762.03	344.27078	−50.20824	19.88	19.26	14.21	6.57 ± 1.73	NM
DES J225709.08-501214.6	57229.33	344.28784	−50.20406	18.25	17.27	44.81	8.47 ± 1.14	NM
DES J225709.39-500956.8	58762.03	344.28915	−50.1658	21.3	20.67	4.12	118.66 ± 2.35	NM
DES J225722.15-501150.7	57229.33	344.34232	−50.19744	19.73	18.91	10.27	−29.24 ± 1.7	NM
DES J225642.95-501741.3	57229.33	344.17897	−50.29482	21.18	20.62	3.16	−148.87 ± 4.97	CM
DES J225643.29-500607.3	57229.33	344.18038	−50.10203	19.74	19.07	17.25	−146.79 ± 1.25	M
	58762.03	344.18038	−50.10203	19.74	19.07	20.64	−146.41 ± 1.24	M
DES J225611.70-500304.8	58762.03	344.04878	−50.05136	19.86	19.31	14.82	−85.61 ± 1.35	NM
DES J225617.78-500309.3	58762.03	344.0741	−50.05259	20.42	19.21	20.75	116.71 ± 1.38	NM
DES J225602.89-500353.8	58762.03	344.01204	−50.06496	20.05	18.61	57.85	−27.75 ± 1.13	NM
DES J225618.15-500405.3	58762.03	344.07565	−50.06815	18.94	18.66	21.47	−31.7 ± 1.3	NM
DES J225615.03-500412.8	58762.03	344.06263	−50.07025	21.7	20.33	12.92	137.47 ± 1.56	NM
DES J225602.84-500414.7	58762.03	344.01186	−50.07076	21.48	21.06	2.6	144.89 ± 5.46	NM
DES J225619.00-500427.2	58762.03	344.0792	−50.07423	18.52	18.02	34.99	−22.89 ± 1.15	NM
DES J225633.63-500426.1	58762.03	344.14012	−50.07393	21.98	20.55	12.11	−6.86 ± 1.67	NM
DES J225626.96-500445.3	58762.03	344.11236	−50.07927	21.77	20.68	5.73	−52.27 ± 4.14	NM
DES J225615.78-500452.8	58762.03	344.06578	−50.08134	21.23	20.9	2.82	−48.25 ± 4.49	NM
DES J225601.68-500459.2	58762.03	344.00702	−50.08312	22.33	20.69	15.95	−5.16 ± 1.46	NM
DES J225603.76-500524.5	58762.03	344.0157	−50.09014	20.94	20.31	5.53	−141.21 ± 1.67	M

Table 2
(Continued)

ID	MJD[a]	R.A. (deg)	Decl. (deg)	g[b] (mag)	r[b] (mag)	S/N	v (km s^{-1})	MEM
DES J225624.48-500540.8	58762.03	344.10202	−50.09468	22.19	20.61	17.33	8.0 ± 1.47	NM
DES J225638.97-500542.4	58762.03	344.1624	−50.09511	20.02	19.43	14.25	20.45 ± 1.82	NM
DES J225644.70-500559.7	58762.03	344.18625	−50.09993	21.95	20.63	11.68	35.89 ± 1.96	NM
DES J225608.69-500603.8	58762.03	344.03622	−50.10107	19.66	19.19	14.54	50.85 ± 1.65	NM
DES J225628.96-500601.9	58762.03	344.12068	−50.10054	20.97	20.0	9.75	89.51 ± 1.83	NM
DES J225613.54-500603.5	58762.03	344.05645	−50.10099	21.05	19.92	14.86	−19.48 ± 1.48	NM
DES J225613.72-500616.4	58762.03	344.05718	−50.10458	16.59	16.75	52.03	156.24 ± 1.25	NM
DES J225649.23-501031.4	58762.03	344.20513	−50.17539	20.79	20.22	6.91	−142.47 ± 1.83	M
DES J225603.42-500617.4	58762.03	344.01426	−50.10483	19.07	18.68	19.51	58.47 ± 1.25	NM
DES J225601.57-500623.0	58762.03	344.00655	−50.1064	21.35	19.93	18.73	76.15 ± 1.32	NM
DES J225617.16-500621.4	58762.03	344.0715	−50.10596	22.54	21.44	2.8	6.05 ± 9.32	NM
DES J225555.38-500642.3	58762.03	343.98078	−50.11175	18.55	17.68	44.28	−70.77 ± 1.14	NM
DES J225626.51-500651.4	58762.03	344.11047	−50.1143	19.98	18.53	51.53	11.07 ± 1.12	NM
DES J225616.50-500651.2	58762.03	344.06877	−50.11425	21.05	20.64	3.98	142.27 ± 3.55	NM
DES J225653.50-500716.3	58762.03	344.22292	−50.12122	21.28	20.22	8.67	27.15 ± 2.49	NM
DES J225657.01-500740.7	58762.03	344.23755	−50.12799	18.09	17.65	43.95	−49.15 ± 1.17	NM
DES J225644.73-500749.0	58762.03	344.1864	−50.1303	21.99	20.7	7.64	98.16 ± 2.55	NM

Notes.
[a] The midpoint MJD of observation.
[b] Quoted magnitudes represent the weighted-average dereddened PSF magnitude derived from the DES DR2 catalog (Flaugher et al. 2015; Morganson et al. 2018; Abbott et al. 2021).
[c] NM indicates nonmembers, CM indicates candidate members (stars with consistent radial velocity, but no derived metallicity), M indicates members (see Section 3.3).

we only report metallicities in Table 3 for stars that are confirmed members of Grus I (defined as radial velocities consistent with membership and a low metallicity; see Section 3.3).

3.3. Identifying Members of Grus I

We identify Grus I members based on their clustered radial velocities and the fact that UFD stars have low metallicities ([Fe/H] $\lesssim -1.5$; Simon 2019). Walker et al. (2016) find that Grus I has a systematic radial velocity of $-140.5^{+2.4}_{-1.6}$ km s^{-1}. We find a significant over-density of stars at a similar radial velocity, as shown in the bottom left panel of Figure 1. We select all stars with radial velocities between −150 and −130 km s^{-1} as an initial sample of 13 possible members. There are no stars with velocities just beyond the threshold of these limits (i.e., no other stars have velocities < -100 km s^{-1}), so it is unlikely that we have excluded any possible members with this velocity cut. We note that all of the stars with radial velocities that are consistent with Grus I membership also have Gaia EDR3 proper motions (Gaia Collaboration et al. 2016, 2021), when available, consistent with the systematic proper motion of Grus I ($\mu_\alpha \cos\delta = 0.07 \pm 0.05$ mas yr^{-1}, $\mu_\delta = -0.29^{+0.06}_{-0.07}$ mas yr^{-1}; McConnachie & Venn 2020). This consistency is illustrated in the bottom right panel of Figure 1.

Of the 13 stars with velocities consistent with Grus I membership, nine have spectra with sufficient signal to noise (S/N > 5) to derive metallicities from the calcium triplet absorption features. We find that eight of these nine stars have very low metallicities ([Fe/H] < -2.0), consistent with UFD membership (see Figures 5 and 6 in Simon 2019). Stars at such low metallicities are unlikely to be foreground Milky Way stars (e.g., Youakim et al. 2020; Chiti et al. 2021a). One star (DES J225643.20-501130.0) has a velocity and proper motion consistent with membership, but a high metallicity of [Fe/H] $= -0.9 \pm 0.38$, which is above the typical metallicity range of UFD stars (no known UFD star has [Fe/H] > -1.0). Based on its high metallicity, we therefore identify this star as a nonmember and exclude it from further analysis, but we note for completeness that none of the primary conclusions of our paper (e.g., orbital properties, Grus I being dark-matter dominated) would change if we were to include this star. As noted in Section 3.2, the metallicity calibration that we employ is only valid for stars at the distance of Grus I. Accordingly, the metallicities of stars that are likely not members of Grus I should be disregarded.

We identify the eight stars with low metallicities ([Fe/H] < -2.0) and velocities consistent with Grus I membership (−150 to −130 km s^{-1}) as confirmed members (M in Table 2). We report the four stars with velocities consistent with membership, but no metallicity measurements as candidate members (CM in Table 2). All other stars are identified as nonmembers. The analysis in Section 4 is performed using the sample of confirmed members.

3.4. Combining Our Sample with Existing Literature Measurements

There are two published studies of Grus I that report velocity and metallicity values of individual member stars (Walker et al. 2016; Ji et al. 2019). We opt to incorporate some of those measurements in our analyses of Grus I to increase our sensitivity to the velocity dispersion of the system and to aid in detecting binary stars. In this subsection, we outline how our velocities and metallicities compare to values presented in those studies, and then discuss whether/how we incorporate their measurements into our study.

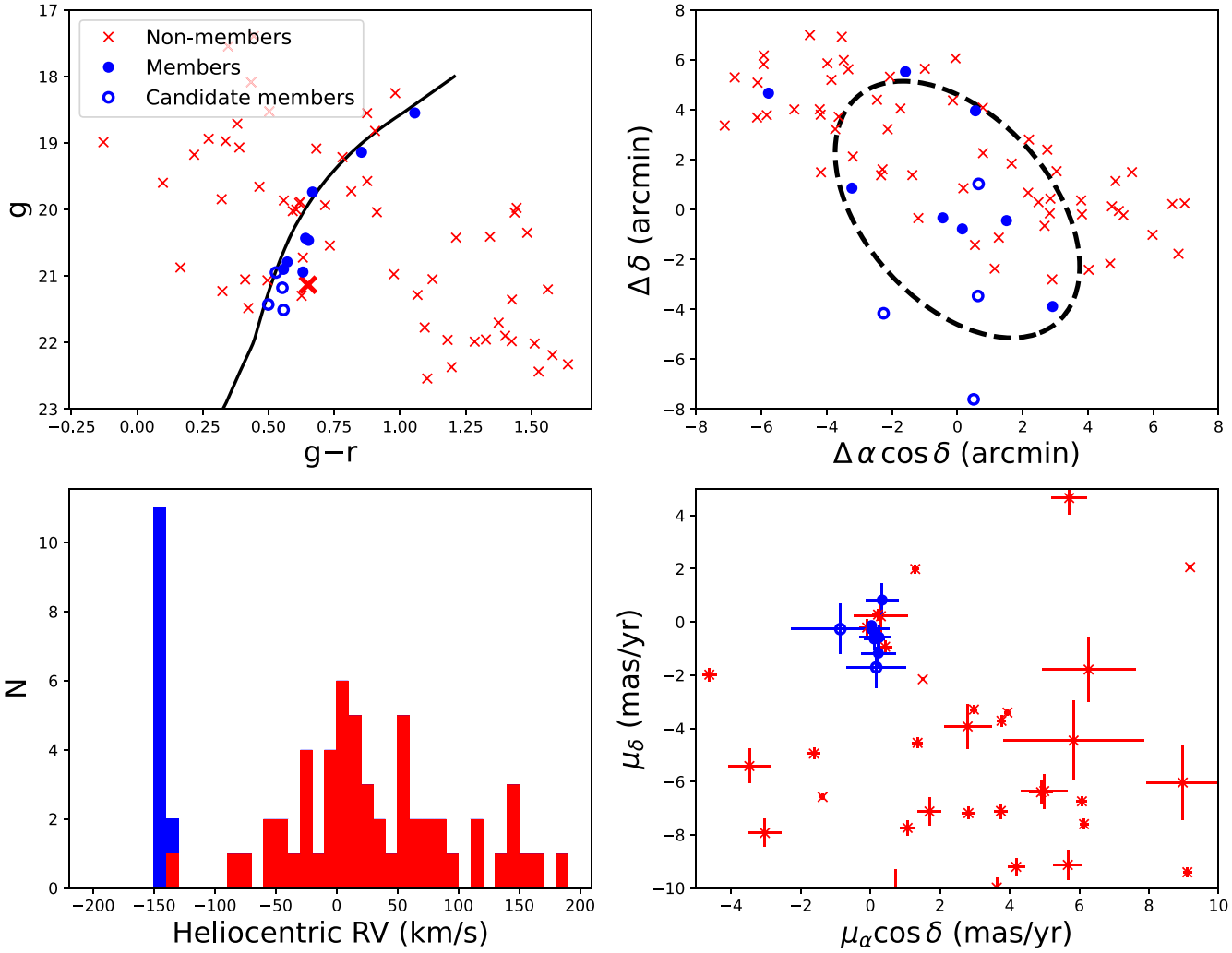

Figure 1. Top left: color–magnitude diagram of stars observed in this study. Confirmed nonmembers of Gru I, as determined by their radial velocities and metallicities (see Section 3.3) are shown as red crosses. Confirmed members of Grus I are shown as filled blue circles. Candidate members (those with velocities consistent with membership, but no metallicity information) are shown as hollow blue circles. DES J225643.20−501130.0, the star with a radial velocity consistent with Grus I membership but a high metallicity ([Fe/H] $= -0.9 \pm 0.38$; see Section 3.3) is indicated by a larger red cross. A 10 Gyr, [Fe/H] $= -2.2$ MIST isochrone (Paxton et al. 2011, 2013, 2015, 2018; Choi et al. 2016; Dotter 2016) is overplotted at the distance modulus of Grus I ($m - M = 20.48$ mag; Cantu et al. 2021) for reference. Top right: spatial distribution of stars observed in this study. The dashed ellipse denotes the Grus I half-light radius presented in Cantu et al. (2021). Bottom left: histogram of velocities of the stars in our sample. The Grus I members clearly cluster between ~ -150 and ~ -135 km s^{-1}. Note that one star (DES J225643.20-501130.0) has a velocity consistent with membership but is listed as a nonmember due to its high metallicity (see paragraph 2 in Section 3.3). Bottom right: Gaia EDR3 (Gaia Collaboration et al. 2016, 2021) proper motions of stars in our sample. The members and candidate members of the Grus I cluster at a systemic proper motion of $\mu_\alpha \cos\delta = 0.07 \pm 0.05$ mas yr^{-1}, $\mu_\delta = 0.25 \pm 0.07$ mas yr^{-1}.

3.4.1. Comparison to Walker et al. (2016)

Walker et al. (2016) used the M2FS multi-fiber instrument on the Magellan/Clay telescope to identify seven likely members of Grus I ($p_{\rm mem} > 0.5$ in their Table 1). We reobserved all of those stars (Gru1-003, Grus-004, Grus1-007, Gru1-023, Gru1-032, Gru1-035, and Gru1-038) in this study. We identify two stars in Walker et al. (2016) (Gru1-022 and Gru1-054) that they do not classify as likely members to be members with our IMACS data (DES J225619.67-500913.1 and DES J225603.76-500524.5, respectively, in Table 2). We find that both stars have IMACS velocities consistent with membership (between -143 and -141 km s^{-1}) and low metallicities ([Fe/H] < -2.5). They likely missed being classified as members in Walker et al. (2016) due to their large velocity uncertainties (19.2 and 87.9 km s^{-1}, respectively) in that study. We note that we identify one likely member in Walker et al. (2016), Gru1-007 (DES J225643.20-501130.0), as a nonmember due to its high IMACS metallicity of [Fe/H] $= -0.9 \pm 0.38$ (see second paragraph in Section 3.3). The star also has a relatively high metallicity of [Fe/H] $= -1.19 \pm 0.42$ in Walker et al. (2016) and is marginally redder than the rest of the Grus I members (as denoted by the larger red cross in the top left panel of Figure 1).

The most notable discrepancy between our study and Walker et al. (2016) is in the metallicity measurements. Six stars we classify as confirmed members have M2FS metallicities in their study (Gru1-003, Gru1-004, Gru1-022, Gru1-032, Gru1-038, and Gru1-054). Our metallicities are, on average, 0.45 ± 0.14 dex lower than their M2FS metallicities. Notably, Gru1-003 (DES J225637.05-501024.8), Gru1-004 (DES J225640.78-501051.4), Gru1-022 (DES J225619.67-500913.1), and Gru1-054 (DES J225603.76-500524.5) have discrepancies in their metallicities of over 0.5 dex; although, Gru1-003, Gru1-022, and Gru1-054 also have highly uncertain M2FS metallicities ($\sigma \geqslant 0.4$ dex) in

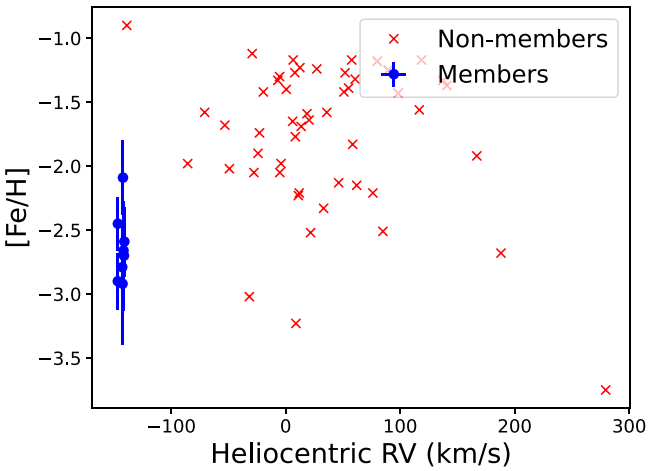

Figure 2. [Fe/H] vs. radial velocities for stars in this study. The members of Grus I clearly cluster at low metallicities ([Fe/H] < -2.0) and at a systematic velocity of ~ -143 km s^{-1}. Note that one star has a velocity consistent with membership but a high metallicity ([Fe/H] -0.9 ± 0.38 dex), and is therefore listed as a nonmember. There are additional candidate members in our sample with velocities consistent with membership (see Section 3.3), but are not shown in this plot as the S/N of their spectra is too low for a metallicity determination.

Walker et al. (2016). The overall offset between our metallicities and those in Walker et al. (2016) is largely explained by the systematic metallicity offset of + 0.32 dex that Walker et al. (2016) added to their metallicities to account for discrepancies with solar values. This offset has been discussed in Chiti et al. (2018) and Ji et al. (2019) as a cause of discrepancy between M2FS metallicities and those derived from high-resolution spectroscopy. Accordingly, we adopt our IMACS calcium triplet-based metallicities in all subsequent analyses.

We find a small, but statistically significant, average velocity offset of $v_{\rm IMACS} - v_{\rm M2FS} = -2.6 \pm 0.8$ km s^{-1} between the IMACS velocities of the Grus I candidate members and the M2FS velocities presented in Walker et al. (2016). After accounting for this offset, there are no $> 2\sigma$ velocity outliers between our studies, reflecting agreement between the M2FS and IMACS velocities. We note that attempting to model this offset as part of our dynamical modeling (see Section 4.1) returns an offset of $v_{\rm IMACS} - v_{\rm M2FS} = -2.8^{+1.0}_{-0.9}$ km s^{-1}, consistent with this more direct estimate of the offset.

We opt to combine our velocities with the M2FS velocities in Walker et al. (2016) to increase the velocity precision of our sample. To account for possible systematic effects when combining measurements from different spectrographs, we implement the likelihood function presented in Minor et al. (2019) in our dynamical analysis in Section 4.1. This likelihood function simultaneously fits for a velocity offset between samples from different spectrographs when deriving dynamical parameters. Additionally, we add a systematic velocity uncertainty of 0.9 km s^{-1} in quadrature to the velocity uncertainties presented in Walker et al. (2016), following the analysis of M2FS velocity uncertainties in Simon et al. (2015). We note that the net effect of both of these corrections is to decrease the significance of any detected velocity dispersion, making these conservative choices with respect to the conclusions of this paper. We present results both with and without these kinematic adjustments in Section 4.1, but the relevant numbers in Table 4 and elsewhere in the paper reflect the steps that are described in this paragraph.

3.4.2. Comparison to Ji et al. (2019)

Ji et al. (2019) used the MIKE spectrograph on Magellan/Clay to obtain high-resolution spectra of Gru1-032 (DES J225658.06−-501357.9) and Gru1-038 (DES J225629.92-500433.3) to derive their detailed abundances. We find excellent agreement (within 0.1 dex) between our metallicities and their metallicities. We opt to use our calcium triplet-based metallicities for these stars in the analysis in this paper to ensure uniformity in how metallicities are derived across our sample. Moreover, given the agreement between the calcium triplet metallicities and the MIKE metallicities, opting for one set over the other does not change any results.

We remeasure the velocities of Gru1-032 (DES J225658.06-501357.9) and Gru1-038 (DES J225629.92-500433.3) from the MIKE spectra presented in Ji et al. (2019), following the steps outlined in Chiti et al. (2022). We derive a velocity of $v_{\rm MIKE} = -139.6 \pm 1.2$ km s^{-1} for Gru1-032, and $v_{\rm MIKE} = -143.3 \pm 1.2$ km s^{-1} for Gru1-038. These are within 4 km s^{-1} of the IMACS and M2FS velocities. We incorporate these velocity measurements in our binarity analysis in Section 3.5.

3.5. Identifying Binary Stars in Grus I

We searched for evidence of binarity in our Grus I candidate members by combining velocity data from this study, Walker et al. (2016), and Ji et al. (2019). Before performing this analysis, we applied an offset of -2.6 km s^{-1} to the velocities in Walker et al. (2016) (see paragraph 3 in Section 3.4.1). We also added a systematic velocity uncertainty of 0.9 km s^{-1} in quadrature to the uncertainties provided in Walker et al. (2016) (see paragraph 4 in Section 3.4.1). The MIKE velocities from Ji et al. (2019) for Gru1-032 (DES J225658.06-501357.9) and Gru1-038 (DES J225629.92-500433.3) were taken as the values presented in the second paragraph of Section 3.4.2. We note that Ji et al. (2019) do not report evidence that either Gru1-032 or Gru1-038 are binaries when comparing their MIKE velocities to M2FS velocities of those stars in Walker et al. (2016).

We tested for binarity by performing a χ^2 test on each star to test the null hypothesis that its velocity is constant over time. The IMACS velocities used for this test are provided in Table 2, and the M2FS and MIKE velocities were included when available. We note that DES J225649.23-501031.4 could not be tested for binarity since it only has a usable radial velocity measurement from one epoch. The same is effectively true for DES J225603.76-500524.5/Gru1-054, which only has an IMACS velocity from one epoch and a highly uncertain M2FS velocity. We find strong evidence ($p = 0.01$) of binarity for Gru1-003 (DES J225637.05-501024.8), and marginal evidence ($p = 0.04$) for Gru1-022 (DES J225619.67-500913.1) if one excludes its uncertain M2FS velocity ($\sigma = 19.2$ km s^{-1}). To be conservative, we exclude velocities from these stars in our dynamical analysis of Grus I in Section 4.1.

Table 3
IMACS Metallicities of Confirmed Grus I Members

ID	R.A. (deg)	Decl. (deg)	g[a] (mag)	r[a] (mag)	[Fe/H]	MEM
DES J225658.06-501357.9	344.24192	−50.23276	18.55	17.49	-2.66 ± 0.19	M
DES J225640.78-501051.4	344.16992	−50.18096	20.43	19.79	-2.09 ± 0.29	M
DES J225629.92-500433.3	344.12467	−50.07593	19.14	18.29	-2.45 ± 0.21	M
DES J225619.67-500913.1	344.08198	−50.15364	20.90	20.34	-2.79 ± 0.28	M
DES J225637.05-501024.8	344.15438	−50.17357	20.46	19.81	-2.59 ± 0.27	M
DES J225643.29-500607.3	344.18038	−50.10203	19.74	19.07	-2.90 ± 0.22	M
DES J225603.76-500524.5	344.0157	−50.09014	20.94	20.31	-2.70 ± 0.43	M
DES J225649.23-501031.4	344.20513	−50.17539	20.79	20.22	-2.92 ± 0.48	M

Note.
[a] Quoted magnitudes represent the weighted-average dereddened PSF magnitude derived from the DES DR2 catalog (Flaugher et al. 2015; Morganson et al. 2018; Abbott et al. 2021).

Table 4
Summary of Properties of Grus I

Row	Quantity	Value
(1)	R.A. (J2000)	$344.166^{+0.007}_{-0.006}$
(2)	decl. (J2000)	$-50.168^{+0.006}_{-0.005}$
(3)	Distance (kpc)	125^{+6}_{-12}
(4)	$m - M$ (mag)	$20.48^{+0.11}_{-0.22}$
(5)	$r_{1/2}$ (arcmin)	$4.16^{+0.54}_{-0.74}$
(6)	Ellipticity	$0.44^{+0.08}_{-0.10}$
(7)	Position angle (degrees)	153^{+8}_{-7}
(8)	$M_{V,0}$	-4.1 ± 0.3
(9)	$r_{1/2}$ (pc)	151^{+21}_{-31}
(10)	$N_{\rm spectroscopic\ members}$	8[a]
(11)	$V_{\rm hel}$ (km s^{-1})	$-143.5^{+1.2}_{-1.2}$ km s^{-1}
(12)	$V_{\rm GSR}$ (km s^{-1})	$-189.4^{+1.2}_{-1.2}$ km s^{-1}
(13)	σ (km s^{-1})	$2.5^{+1.3}_{-0.8}$ km s^{-1}
(14)	Mass ($M_\odot$)	$8^{+12}_{-4} \times 10^5$
(15)	M/L_V ($M_\odot/L_\odot$)	440^{+650}_{-250}
(16)	Mean [Fe/H]	-2.62 ± 0.11
(17)	$\mu_\alpha \cos\delta$ (mas yr^{-1})	0.07 ± 0.05 mas yr^{-1}
(18)	μ_δ (mas yr^{-1})	-0.25 ± 0.07 mas yr^{-1}
(19)	Orbital pericenter (kpc)	49^{+27}_{-23} kpc[b]
(20)	Orbital apocenter (kpc)	205^{+58}_{-24} kpc[b]
(21)	$\log_{10} J(0.^\circ2)$ (GeV^2 cm^{-5})	$16.4^{+0.8}_{-0.7}$
(22)	$\log_{10} J(0.^\circ5)$ (GeV^2 cm^{-5})	$16.5^{+0.8}_{-0.7}$

Notes. Columns (1)−(9) are from Cantu et al. (2021); Columns (19) and (20) are from Pace et al. (2022); all other columns are from this study.
[a] Only includes stars with a confirmed low metallicity from IMACS spectroscopy.
[b] Taken from Pace et al. (2022), which presented Grus I orbital parameters including the effect of the Large Magellanic Cloud (LMC), but with the systemic radial velocity in Walker et al. (2016). Our updated systemic velocity should negligibly affect these values; see Section 4.4 for further discussion.

4. Discussion

In this section, we answer four questions about Grus I: (1) What is its dynamical mass and is it dark-matter dominated? (2) Does Grus I follow the mass–metallicity and metallicity-luminosity relations for dwarf galaxies? (3) What is the viability of using Grus I for searches for dark-matter interactions? And (4) What is the orbital history of Grus I? We then conclude by comparing our results to those currently in the literature. In subsequent analysis, we use the IMACS metallicities and velocities of confirmed Grus I members (as described in Section 3.3), supplemented by their M2FS velocity measurements in Walker et al. 2016 (see Section 3.4.1).

4.1. Dynamical Mass of Grus I

We derive the dynamical mass within a half-light radius of Grus I using the estimator presented in Wolf et al. (2010):

$$M(r_{1/2}) \simeq \left(\frac{\langle\sigma^2_{\rm los}\rangle}{\rm km^2\ s^{-2}}\right)\left(\frac{R_e}{\rm pc}\right) M_\odot \quad (1)$$

in which $\langle\sigma^2_{\rm los}\rangle$ is the squared line-of-sight velocity dispersion and $R_{\rm e}$ is the two-dimensional projected half-light radius. We adopt $R_{\rm e} = 151^{+21}_{-31}$ pc (Cantu et al. 2021) in all subsequent calculations.

We derive the velocity dispersion of Grus I using a maximum-likelihood approach on a joint sample of IMACS and M2FS (Walker et al. 2016) velocity measurements. We restrict our sample to confirmed members (as described in the last paragraph of Section 3.3) and stars that do not show evidence of binarity (see Section 3.5). These restrictions result in a sample of six stars for the velocity dispersion derivation. Three of these stars (DES J225658.06, DES J225640.78, and DES J225629.92 in Table 3) have precise M2FS velocities (uncertainties < 2 km s^{-1}) in Walker et al. (2016). To self-consistently incorporate these M2FS velocities with our IMACS velocities when deriving the velocity dispersion, we implement the likelihood function presented in Equations (2) and 3 of Minor et al. (2019). This likelihood simultaneously fits for velocity offsets in velocities from different spectrographs when deriving the systemic velocity and velocity dispersion. We implemented this likelihood function in `emcee` (Foreman-Mackey et al. 2013, 2019), and initialized our sample with 100 walkers with a uniform prior on the velocity offset and systemic velocity, and a Jeffreys Prior on the velocity dispersion. The resulting corner plot after 2000 steps is shown in the left panels of Figure 3.

From this MCMC analysis (and as can be seen in Figure 3), we derive a systemic velocity of -143.5 ± 1.2 km s^{-1}, a velocity dispersion of $2.5^{+1.3}_{-0.8}$ km s^{-1}, and a velocity offset between measurements from the M2FS and IMACS spectrographs of $-2.8^{+1.0}_{-0.9}$ km s^{-1}. The 95% confidence interval (CI) of the velocity dispersion is 1.2−6.2 km s^{-1}, demonstrating that we clearly resolve a

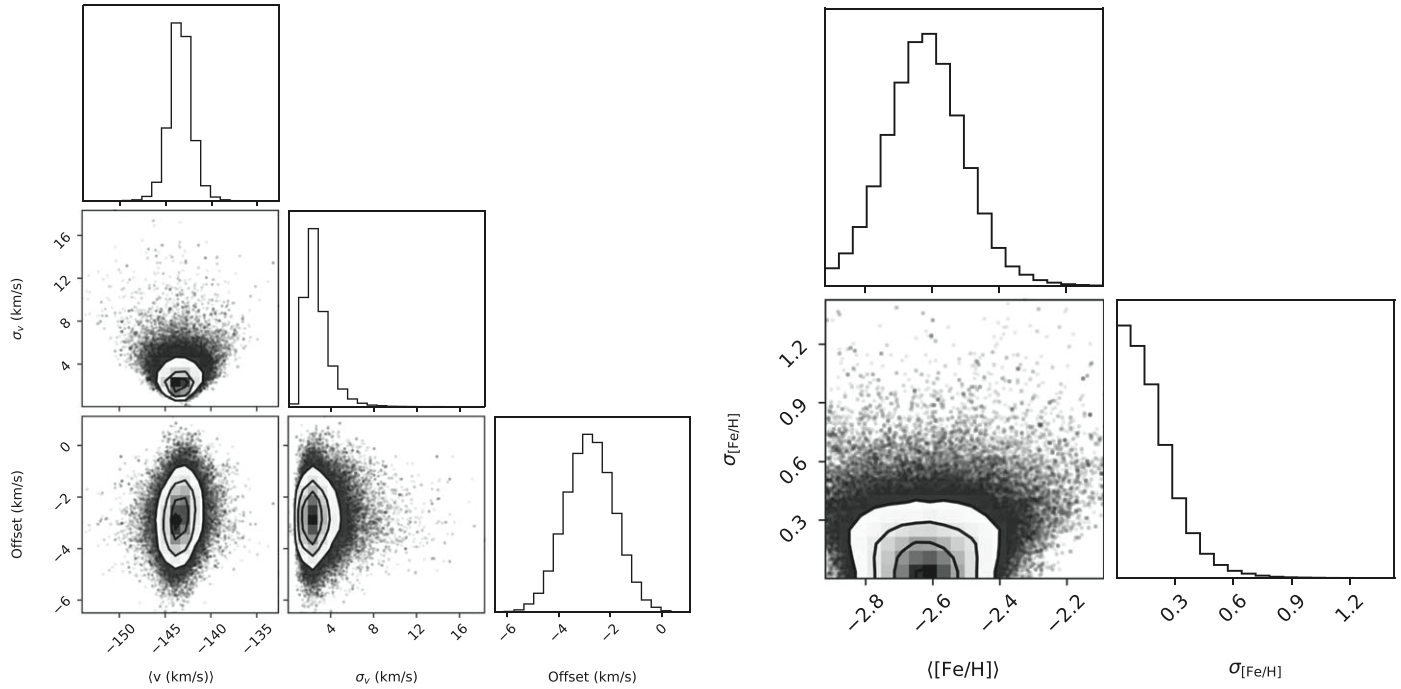

Figure 3. Left panels: corner plot from our Markov Chain Monte Carlo (MCMC) analysis to determine the systemic radial velocity and velocity dispersion of Grus I, while jointly fitting for the velocity offset between the M2FS and IMACS spectrographs (see Section 4.1). We determine a systematic velocity of -143.5 ± 1.2 km s^{-1} and a velocity dispersion of $2.5^{+1.3}_{-0.8}$ km s^{-1}, confirming Grus I to be dark-matter dominated (>80 $M_\odot/L_\odot$ from the 95% CI; see Section 4.1) as is typical of UFDs. Right panels: corner plot from our MCMC analysis to determine the mean metallicity and metallicity dispersion of Grus I. We find that Grus I has a low $\langle$[Fe/H]$\rangle = -2.62 \pm 0.11$, also as is typical of UFDs, and places an upper limit on the metallicity dispersion of $\sigma_{[Fe/H]} < 0.44$.

velocity dispersion at a $> 2\sigma$ level. This dispersion results in a dynamical mass within a half-light radius of $8^{+12}_{-4} \times 10^5\ M_\odot$ (95% CI of 1.7×10^5 to $5.2 \times 10^6\ M_\odot$). The corresponding mass-to-light ratio is $440^{+650}_{-250}\ M_\odot/L_\odot$ (95% CI of $80-3000\ M_\odot/L_\odot$) using the absolute magnitude of $M_V = -4.1 \pm 0.3$ reported in Cantu et al. (2021). This establishes that Grus I is a canonical, dark-matter-dominated UFD.

To ensure this conclusion is robust to how we combined the M2FS and IMACS velocities, we repeat the above analysis with several modifications and present the results here. When including the metal-rich star at the systemic velocity of Grus I in our analysis (DES J225643.20-501130.0; see paragraph 2 in Section 3.3), we derive a systemic velocity of $-143.1^{+1.2}_{-1.0}$ km s^{-1} and a velocity dispersion of $2.5^{+1.3}_{-0.7}$ km s^{-1}. If we do not add the systematic velocity uncertainty of 0.9 km s^{-1} to the M2FS velocities and repeat the above analysis, we derive a systemic velocity of $-143.5^{+1.3}_{-1.2}$ km s^{-1} and a velocity dispersion of $2.7^{+1.3}_{-0.8}$ km s^{-1}. If we choose to combine the M2FS and IMACS velocities by just manually adding an offset of -2.6 km s^{-1} to the M2FS velocities, taking a weighted average with the IMACS velocities, and repeating the analysis, we derive a systematic velocity of $-143.5^{+1.2}_{-1.1}$ km s^{-1} and a velocity dispersion of $2.5^{+1.2}_{-0.8}$ km s^{-1}. If we include the two binary candidates (DES J225637.05-501024.8 and DES J225619.67-500913.1) using their mean velocities, we derive a dispersion of $2.3^{+0.9}_{-0.7}$ km s^{-1}; similarly, if we also include the four candidate members (see Section 3.3), we derive a velocity dispersion of $2.1^{+0.7}_{-0.6}$ km s^{-1}. Including the MIKE velocities of DES J225658.06-501357.9 and DES J225629.92-500433.3 still results in a significant dispersion of $2.3^{+1.2}_{-0.7}$ km s^{-1}. The only case that results in the system not being dark-matter dominated at the 2σ level is when only the IMACS velocities of the six confirmed members are used; this sample results in a dispersion of $2.1^{+1.3}_{-0.9}$ km s^{-1} and a 95% CI on the mass-to-light ratio from 3 to 2400 $M_\odot/L_\odot$. However, in the latter case, the system again becomes clearly M/L_V dominated when a uniform prior is used instead of Jeffrey's prior when deriving the dispersion. Accordingly, in all but one case, none of the Grus I-derived properties are meaningfully sensitive to our choice of how to combine the M2FS and IMACS data sets. For completeness, we also note that tests with mock data show that we can recover the correct velocity dispersion of Grus I with a sample of six stars, with similar uncertainties to what we obtained.

4.2. Metallicity Properties of Grus I

We derive the mean metallicity and metallicity dispersion of Grus I using the metallicities of its eight confirmed members (see Table 3). We implement the exact same MCMC approach and implementation as in Section 4.1, but instead just use the metallicity-related terms in the likelihood function in Equation (4) of Walker et al. (2016) assuming no metallicity gradient. This likelihood models the metallicity distribution as a Gaussian with a mean metallicity $\mu_{[Fe/H]}$ and a metallicity dispersion $\sigma_{[Fe/H]}$.

We derive that Grus I has a mean metallicity of $\mu_{[Fe/H]} = -2.62 \pm 0.11$ and place a 2σ upper limit on the metallicity dispersion of $\sigma_{[Fe/H]} < 0.45$ (see right panels in Figure 3). The mean metallicity places Grus I exactly on the mass–metallicity and metallicity-luminosity relation for UFDs (see Figure 4), affirming its status as a UFD. The agreement between the location of Grus I on these planes and the population of UFDs also suggests that Grus I did not

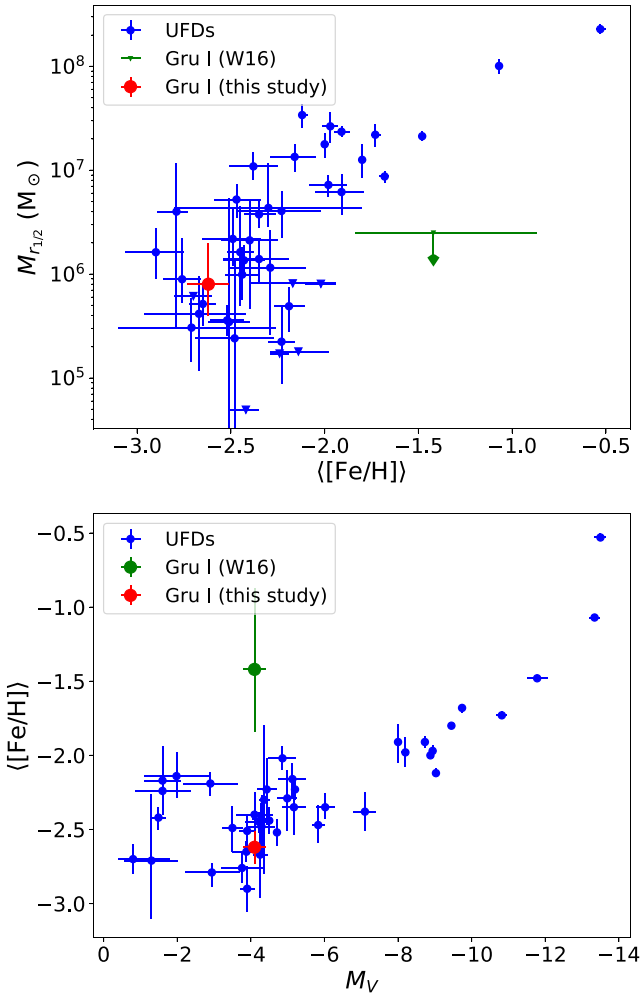

Figure 4. Top: UFD dynamical masses as a function of UFD mean metallicity (see Appendix A for a full list of references). The Grus I properties derived in Walker et al. (2016) are shown in green. The properties derived in this study are shown in red. Our derived metallicity and dynamical mass (see Table 4) place Gru I in the expected mass–metallicity regime for UFDs. Bottom: same as above, but for the metallicity-luminosity relation. Our results place Grus I exactly on the UFD trend.

experience any unique effects from, e.g., tidal stripping relative to the UFD population. The lack of a resolved metallicity dispersion in Grus I is most likely due to the small sample size of members, for it is not uncommon for UFDs to show metallicity dispersions below our upper limit of 0.45 dex (see Supplemental Table 1 in Simon 2019).

For completeness, we note that including the metal-rich star at the systemic velocity of Grus I (DES J225643.20-501130.0; see paragraph 2 in Section 3.3) returns a mean metallicity of $-2.46^{+0.21}_{-0.19}$ dex and, unsurprisingly, a resolved metallicity dispersion of $0.53^{+0.25}_{-0.19}$ dex. Consequently, even if we were to assume that DES J225643.20-501130.0 were a member, Grus I would still have an overall low metallicity in line with other UFDs (see Figure 4). The hypothetically resolved metallicity dispersion would also only strengthen the conclusion that Grus I is a UFD. High-resolution spectroscopic follow-up of DES J225643.20-501130.0 is not easily obtainable due to its faintness ($g \sim 19.5$), but would remove any ambiguity in the star's association with Grus I by allowing neutron-capture element abundances to be derived (e.g., Ji et al. 2019).

4.3. J-factor Calculations for Grus I

We compute the astrophysical component of the dark-matter annihilation flux (J factor) and decay flux (D factor) following Pace & Strigari (2019). Briefly, this involves comparing the observed velocity distribution to a theoretical velocity dispersion from solutions of the spherical Jeans equations (e.g., Bonnivard et al. 2015; Geringer-Sameth et al. 2015). In the Jeans modeling, we assume a Navarro–Frenk–White dark-matter profile, a Plummer distribution for the stellar component, and that the stellar anisotropy is constant with radius. For more details see Pace & Strigari (2019).

From the combined IMACS and M2FS data set, we compute integrated J factors of $\log_{10} J = 16.2^{+0.8}_{-0.7}$, $16.4^{+0.8}_{-0.7}$, $16.5^{+0.8}_{-0.7}$ within solid angles of $0.^\circ1$, $0.^\circ2$, and $0.^\circ5$ in logarithmic units of $\mathrm{GeV^2\,cm^{-5}}$ and compute integrated D factors of $\log_{10} D = 16.3 \pm 0.4$, 16.7 ± 0.4, 17.2 ± 0.5 within solid angles of $0.^\circ1$, $0.^\circ2$, and $0.^\circ5$ in logarithmic units of $\mathrm{GeV\,cm^{-2}}$. The J factor scales as $J \propto \sigma^4 / r_{1/2} d^2$ and the low-velocity dispersion and large size lead to a small dark-matter flux from Grus I (Pace & Strigari 2019). Due to the low dark-matter density of Grus I, the J factor is quite small compared to other UFDs at similar distances and has one of the lowest J factors (second to Crater II Caldwell et al. 2017). For reference, the largest J factors are $\log_{10} J \sim 19$ for Segue 1 and Reticulum II (Pace & Strigari 2019). If Grus I were at its orbital pericenter (~50 kpc) the J factor would increase by a factor of ~7 but Grus I would still remain as one of the lowest J factors for Milky Way satellites. Grus I will likely only be useful in stacked analysis for searches for dark-matter annihilation.

4.4. Orbital History and Central Density of Grus I

We initially follow the steps described in Section 4.4 of Simon et al. (2020) to model the orbit of Grus I. We first derive a systemic proper motion for Grus I of $\mu_\alpha \cos\delta = 0.07 \pm 0.05$ mas yr^{-1} and $\mu_\delta = -0.25 \pm 0.07$ mas yr^{-1} by taking the inverse-variance weighted average of the Gaia EDR3 proper motions (Gaia Collaboration et al. 2016, 2021) of its eight confirmed members. This systemic proper motion agrees exactly with the result from the mixture model approach in Pace et al. (2022) and is consistent with the Grus I proper motion of $\mu_\alpha \cos\delta = 0.07 \pm 0.05$ and $\mu_\delta = -0.27 \pm 0.07$ mas yr^{-1} reported in Battaglia et al. (2022). This systemic proper motion, coupled with the radial velocity, distance, R.A., and decl. in Table 4 provides 6D phase space information from which to calculate the orbit of Grus I given a Galactic potential.

As a first pass, we initialized `orbit` instances in the `galpy` package (Bovy 2015) for Grus I in an `MWPotential2014` potential, which had been modified to increase the halo mass to $1.6 \times 10^{12}\,M_\odot$ following, e.g., Carlin & Sand (2018). We note that this potential does not include the effect of the LMC, and so the orbital parameters in this paragraph are shown for comparison purposes only and should not supplant those in, e.g., Pace et al. (2022) (see discussion in the next paragraph). We generate 10,000 instances of these orbits, sampling from the distance, proper motion, and velocity measurements in Table 4 as Gaussian distributions, and integrate forward and backward for 2 Gyr. We derive a pericenter of 20^{+13}_{-10} kpc, and find that Grus I will pass its pericenter in ~400 Myr. Additionally, we find that Grus I has not had a close encounter (within ~10 kpc) with the LMC, suggesting that it is not an LMC satellite. This is in agreement with previous studies (e.g.,

Kallivayalil et al. 2018; Battaglia et al. 2022), and our pericenter is consistent with the non-LMC Grus I pericenter in Pace et al. (2022) of 28^{+16}_{-13} kpc. This suggests that our updated Grus I radial velocity relative to Walker et al. (2016) should not have a significant effect on the Grus I orbital parameters.

Pace et al. (2022) re-derive the orbital parameters of Grus I while accounting for the gravitational effects of the LMC. Given their inclusion of the LMC, the parameters in that study should supersede the parameters presented in the previous paragraph. We note that their assumed systemic Grus I radial velocity (-140.5 ± 2.0 km s^{-1} from Walker et al. 2016) and proper motions ($\mu_{\alpha} \cos\delta = 0.07 \pm 0.05$ and $\mu_{\delta} = -0.25 \pm 0.07$ mas yr^{-1}) are comparable to what is presented in Table 4. Indeed, the only parameter that is marginally different is the systemic velocity of Grus I (by 3 km s^{-1}). The effect of this difference will be negligible compared to uncertainties arising from the proper motion of the system, meaning the orbit results in Pace et al. (2022) from including the LMC should be comparable to what one would derive when assuming the Grus I parameters in this study. Pace et al. (2022) find that the Grus I orbit pericenter increases to 49^{+27}_{-23} kpc (see Figure 4 in Pace et al. 2022) when including the effect of the LMC, and that Grus I is still likely unassociated with the LMC.

Intriguingly, the derived central density of Grus I from the Jeans modeling in Section 4.3 is $\rho_{1/2} \sim 3.5^{+5.7}_{-2.1} \times 10^7$ $M_{\odot}$ kpc^{-3}, among the lowest of UFDs that show no signs of tidal disruption (see Figure 5 in Pace et al. 2022). Given the large pericenter of the orbit of Grus I when including the influence of the LMC, its density is unlikely to be significantly further suppressed on a short timescale by future tidal encounters with the Milky Way. As increasing samples of UFDs are discovered and characterized with upcoming surveys (e.g., LSST), models of the formation and evolution of UFDs will need to explain this diversity of inner densities independently of mass loss scenarios from interactions with the Milky Way (e.g., Ji et al. 2021).

4.5. Comparison to Previous Studies

We derive metallicity and kinematic properties of Grus I that are more precise than those currently in the literature, largely due to our addition of a comprehensive sample of IMACS velocities and metallicities. In particular, we resolve a velocity dispersion ($\sigma = 2.5^{+1.3}_{-0.8}$ km s^{-1}), find that Grus I is a dark-matter-dominated system ($M_{1/2}(r_h) = 8^{+12}_{-4} \times 10^5$ $M_{\odot}$ and $M/L_V = 440^{+650}_{-250}$ $M_{\odot}/L_{\odot}$), and that Grus I has a mean metallicity ($\langle$[Fe/H]$\rangle = -2.62 \pm 0.11$ dex) that is among the lowest of known UFDs (see Figure 4).

Our derived quantities are also generally consistent with the existing upper limits and quantities in the literature. Walker et al. (2016) derive a systemic radial velocity of $-140.5^{+2.4}_{-1.6}$ km s^{-1}, a dispersion of $\sigma_{v_{\rm los}} < 9.8$ km s^{-1} and a dynamical mass of $M_{1/2}(r_h) < 2.5 \times 10^6$ $M_{\odot}$, which are consistent with our quantities. Their Grus I mean metallicity ($\langle$[Fe/H]$\rangle = -1.42^{+0.55}_{-0.42}$) is just consistent at the 2σ level with our derived metallicity if one also accounts for the +0.32 dex offset that was applied to M2FS metallicities (see discussion in paragraph 2 of Section 3.4.1). Zoutendijk et al. (2021) derive a systemic velocity of $-139.2^{+6.1}_{-5.2}$ km s^{-1}, a velocity dispersion of $10.4^{+9.3}_{-5.1}$ km s^{-1}, and a mass and mass-to-light ratio of $M_{1/2}(r_{1/2}) = 1.1^{+2.1}_{-0.8} \times 10^6$ $M_{\odot}$ – $1.7^{+2.9}_{-1.2} \times 10^6$ $M_{\odot}$ and $7.4^{+60.2}_{-6.3} \times 10^3$ $M_{\odot}$ $L_{\odot}^{-1}$ – $3.2^{+33.9}_{-2.7} \times 10^4 M_{\odot}$ $L_{\odot}^{-1}$, respectively. These dispersion, mass, and mass-to-light values are systematically higher than our derived quantities, but still consistent within 2σ. We highlight that our larger sample of members than the previous M2FS study, and our precise IMACS spectroscopic metallicity values allow us to cleanly separate Grus I members from the foreground. This leads to more robust constraints on the dynamical properties of the system, through less uncertain kinematic parameters. We thus conclusively show that Grus I is a canonical low metallicity, dark-matter-dominated UFD.

5. Conclusion

We present a comprehensive study of the metallicity and kinematic properties of Grus I, confirming it to be a very metal-poor ($\langle$[Fe/H]$\rangle = -2.62 \pm 0.11$ dex), dark-matter-dominated ($M/L_V = 440^{+650}_{-250}$ $M_{\odot}/L_{\odot}$) UFD. We combine existing M2FS spectroscopic measurements of Grus I members in the literature (Walker et al. 2016) with comprehensive IMACS spectroscopic follow-up of known and newly discovered members. With our updated sample of eight confirmed Grus I members, we significantly revise downward the existing spectroscopic metallicity of Grus I ($\langle$[Fe/H]$\rangle = -1.42^{+0.55}_{-0.42}$; Walker et al. 2016) and consequently find that Grus I is one of the lowest metallicity UFDs. We also resolve a velocity dispersion of $\sigma = 2.5^{+1.3}_{-0.8}$ km s^{-1}, consistent with the existing upper limit of $\sigma_{v_{\rm los}} < 9.8$ km s^{-1} from Walker et al. (2016) and below the previously reported dispersion of $10.4^{+9.3}_{-5.1}$ km s^{-1} in Zoutendijk et al. (2021). Our analysis corroborates existing hints in the literature from, e.g., neutron-capture element abundances (Ji et al. 2019) that Grus I is a UFD.

We note that our additional IMACS observations robustly constrain the properties of Grus I in two ways. First, the velocity baseline of our IMACS observations extends from 2015 to 2021 and all of the candidate members in Walker et al. (2016) were reobserved. This data set, when coupled with velocities from Walker et al. (2016) and MIKE observations in Ji et al. (2019), allows us to test nearly every Grus I member for binarity (see Section 3.5). We identified two Grus I members as possible binaries and excluded them from subsequent dynamical analysis to avoid biases. Second, our IMACS metallicities are more precise than the bulk of existing Grus I metallicities (see Section 3.4.1), which allows for a more accurate determination of the metallicity properties of Grus I and also a cleaner separation of members from the foreground. From our revised analyses, it is clear that Grus I is not an anomalous UFD. We find no evidence of significant mass loss through tidal interactions, and our metallicity measurements place the galaxy on the UFD mass–metallicity and mass-luminosity relations (see Figure 4). Table 4 lists the full properties of Grus I.

We perform an orbital analysis of Grus I in a simple Milky Way potential, and find that Grus I is unlikely to be associated with the LMC. As described in Pace et al. (2022), the Grus I orbital properties are notably affected by including gravitational effect of the LMC by, e.g., shifting its pericenter to ~50 kpc. However, those updated parameters still show no evidence that Grus I is tidally disrupting or associated with the LMC (Pace et al. 2022).

Interestingly, the central density of Grus I ($\rho_{1/2} \sim 3.5^{+5.7}_{-2.1} \times 10^7$ $M_{\odot}$ kpc^{-3}) is among the lowest of UFDs that are not known to be tidally disrupting (see Figure 5 in Pace et al. 2022). Only

Grus II has a lower density and Columba I has an upper limit that is a factor of 3 larger; however, a number of classical dwarf galaxies (e.g., Ant 2, Crater 2, and Fornax) have lower densities. Despite its low density, it is unlikely that Grus I is disrupting given its orbit and agreement with UFD scaling relations (see Section 4.2). Much as models of UFD evolution attempt to explain the diversity in the outskirts of these systems (e.g., Chiti et al. 2021b; Tarumi et al. 2021), explaining the variations of their properties in general (e.g., inner densities) will also be key to understanding the evolution of these relic galaxies. Future surveys (e.g., LSST) have the potential to discover large samples of faint systems in the Milky Way and the Local Group (e.g., Mutlu-Pakdil et al. 2021) to assess the full range of their properties.

A.C. is supported by a Brinson Prize Fellowship at the University of Chicago/KICP. J.D.S. is supported in part by the National Science Foundation under grant AST-1714873. A.F. acknowledges support from NSF grant AST-1716251. A.B.P. is supported by NSF grant AST-1813881. T.S.L. acknowledges financial support from the Natural Sciences and Engineering Research Council of Canada (NSERC) through grant RGPIN-2022-04794.

This work has made use of data from the European Space Agency (ESA) mission Gaia (https://www.cosmos.esa.int/gaia), processed by the Gaia Data Processing and Analysis Consortium (DPAC, https://www.cosmos.esa.int/web/gaia/dpac/consortium). Funding for the DPAC has been provided by national institutions, in particular the institutions participating in the Gaia Multilateral Agreement.

This project used public archival data from the Dark Energy Survey (DES). Funding for the DES Projects has been provided by the U.S. Department of Energy, the U.S. National Science Foundation, the Ministry of Science and Education of Spain, the Science and Technology Facilities Council of the United Kingdom, the Higher Education Funding Council for England, the National Center for Supercomputing Applications at the University of Illinois at Urbana-Champaign, the Kavli Institute of Cosmological Physics at the University of Chicago, the Center for Cosmology and Astro-Particle Physics at the Ohio State University, the Mitchell Institute for Fundamental Physics and Astronomy at Texas A&M University, Financiadora de Estudos e Projetos, Fundação Carlos Chagas Filho de Amparo à Pesquisa do Estado do Rio de Janeiro, Conselho Nacional de Desenvolvimento Científico e Tecnológico and the Ministério da Ciência, Tecnologia e Inovação, the Deutsche Forschungsgemeinschaft, and the Collaborating Institutions in the Dark Energy Survey.

The Collaborating Institutions are Argonne National Laboratory, the University of California at Santa Cruz, the University of Cambridge, Centro de Investigaciones Energéticas, Medioambientales y Tecnológicas-Madrid, the University of Chicago, University College London, the DES-Brazil Consortium, the University of Edinburgh, the Eidgenössische Technische Hochschule (ETH) Zürich, Fermi National Accelerator Laboratory, the University of Illinois at Urbana-Champaign, the Institut de Ciències de l'Espai (IEEC/CSIC), the Institut de Física d'Altes Energies, Lawrence Berkeley National Laboratory, the Ludwig-Maximilians Universität München and the associated Excellence Cluster Universe, the University of Michigan, the National Optical Astronomy Observatory, the University of Nottingham, The Ohio State University, the OzDES Membership Consortium, the University of Pennsylvania, the University of Portsmouth, SLAC National Accelerator Laboratory, Stanford University, the University of Sussex, and Texas A&M University.

Based in part on observations at Cerro Tololo Inter-American Observatory, National Optical Astronomy Observatory, which is operated by the Association of Universities for Research in Astronomy (AURA) under a cooperative agreement with the National Science Foundation.

This research has made use of NASA's Astrophysics Data System Bibliographic Services (Wenger et al. 2000).

Software: COSMOS reduction pipeline (Dressler et al. 2011; Oemler et al. 2017), astropy (Astropy Collaboration et al. 2013, 2018), emcee (Foreman-Mackey et al. 2013, 2019), galpy (Bovy 2015).

Appendix A
References for Dwarf Galaxy Data in Figure 4

Here, we list the references for the masses, metallicities, and luminosities of the dwarf galaxies plotted in Figure 4: Majewski et al. (2003), Battaglia et al. (2006), Simon & Geha (2007), Bellazzini et al. (2008), de Jong et al. (2008), Mateo et al. (2008), Okamoto et al. (2008), Koch et al. (2009), Walker et al. (2009a), Walker et al. (2009b), Simon et al. (2011), Willman et al. (2011), Fabrizio et al. (2012), Kirby et al. (2013a), Kirby et al. (2013b), Frebel et al. (2014), Bechtol et al. (2015), Drlica-Wagner et al. (2015), Koposov et al. (2015b), Kim et al. (2015), Kirby et al. (2015), Simon et al. (2015), Crnojevic et al. (2016), Ji et al. (2016), Kim et al. (2016), Torrealba et al. (2016a), Torrealba et al. (2016b), Collins et al. (2017), Caldwell et al. (2017), Kirby et al. (2017), Li et al. (2017), Mucciarelli et al. (2017), Simon et al. (2017), Spencer et al. (2017), Chiti et al. (2018), Koposov et al. (2018), Longeard et al. (2018), Li et al. (2018b), Munoz et al. (2018), Mutlu-Pakdil et al. (2018), Torrealba et al. (2018), Simon (2019), Simon et al. (2020), Jenkins et al. (2021), Longeard et al. (2021), Chiti et al. (2022), Cerny et al. (2022).

Appendix B
Compilation of Velocity Measurements of Grus I Members

In Table 5, we compile all velocity measurements of confirmed Grus I members in this work with their velocity measurements in Walker et al. (2016). Note that a zero-point offset of -2.6 km s^{-1} has been applied to the velocities in Walker et al. (2016) to account for an offset between M2FS and IMACS velocities (see Section 3.4.1).

Table 5
Compilation of Velocity Measurements for Confirmed Grus I Members

Name	MJD[a]	R.A. (deg) (J2000)	Decl. (deg) (J2000)	Instrument	v_{helio} (km s^{-1})	v_{err} (km s^{-1})	Reference
DES J225658.06-501357.9	57222.3	344.24192	−50.23276	M2FS	−141.0[b]	0.4	Gru1-032 in Walker et al. (2016)
	57229.3	344.24192	−50.23276	IMACS	−140.88	1.11	This work
	58762.0	344.24192	−50.23276	IMACS	−141.59	1.11	This work
	59471.0	344.24192	−50.23276	IMACS	−143.32	1.13	This work
DES J225640.78-501051.4	57222.3	344.16992	−50.18096	M2FS	−142.0[b]	1.4	Gru1-004 in Walker et al. (2016)
	58762.0	344.16992	−50.18096	IMACS	−142.49	1.46	This work
	59471.0	344.16992	−50.18096	IMACS	−140.68	2.11	This work
DES J225629.92-500433.3	57222.3	344.12467	−50.07593	M2FS	−146.9[b]	0.8	Gru1-038 in Walker et al. (2016)
	57229.3	344.12467	−50.07593	IMACS	−147.39	1.15	This work
	58762.0	344.12467	−50.07593	IMACS	−146.38	1.14	This work
	59471.0	344.12467	−50.07593	IMACS	−144.72	1.26	This work
DES J225619.67-500913.1	57222.3	344.08198	−50.15364	M2FS	−143.8	19.2	Gru1-022 in Walker et al. (2016)
	57229.3	344.08198	−50.15364	IMACS	−146.35	2.39	This work
	58762.0	344.08198	−50.15364	IMACS	−139.67	2.24	This work
DES J225637.05-501024.8	57222.3	344.15438	−50.17357	M2FS	−140.2	3.9	Gru1-003 in Walker et al. (2016)
	57229.3	344.15438	−50.17357	IMACS	−135.25	2.13	This work
	58762.0	344.15438	−50.17357	IMACS	−143.08	1.58	This work
DES J225643.29-500607.3	57229.3	344.18038	−50.10203	IMACS	−146.79	1.25	This work
	58762.0	344.18038	−50.10203	IMACS	−146.41	1.24	This work
DES J225603.76-500524.5	57222.3	344.01570	−50.09014	M2FS	−128.0	87.9	Gru1-054 in Walker et al. (2016)
	58762.03	344.0157	−50.09014	IMACS	−141.21	1.67	This work
DES J225649.23-501031.4	58762.0	344.20513	−50.17539	IMACS	−142.47	1.83	This work

Notes.
[a] Defined as the MJD at the midpoint of observation. For velocities reported in Walker et al. (2016), we list the MJD derived from Table 1 in that study.
[b] Offset of −2.6 km s^{-1} has been applied to account for a zero-point offset between M2FS and IMACS velocities (see paragraph 3 in Section 3.4.1).

ORCID iDs

Anirudh Chiti https://orcid.org/0000-0002-7155-679X
Joshua D. Simon https://orcid.org/0000-0002-4733-4994
Anna Frebel https://orcid.org/0000-0002-2139-7145
Andrew B. Pace https://orcid.org/0000-0002-6021-8760
Alexander P. Ji https://orcid.org/0000-0002-4863-8842
Ting S. Li https://orcid.org/0000-0002-9110-6163

References

Abbott, T. M. C., Abdalla, F. B., Allam, S., et al. 2018, ApJS, 239, 18
Abbott, T. M. C., Adamow, M., Aguena, M., et al. 2021, ApJS, 255, 20
Abdallah, H., Adam, R., Aharonian, F., et al. 2020, PhRvD, 102, 062001
Astropy Collaboration, Price-Whelan, A. M., Sipőcz, B. M., et al. 2018, AJ, 156, 123
Astropy Collaboration, Robitaille, T. P., Tollerud, E. J., et al. 2013, A&A, 558, A33
Battaglia, G., Taibi, S., Thomas, G. F., & Fritz, T. K. 2022, A&A, 657, A54
Battaglia, G., Tolstoy, E., Helmi, A., et al. 2006, A&A, 459, 423
Bechtol, K., Drlica-Wagner, A., Balbinot, E., et al. 2015, ApJ, 807, 50
Bellazzini, M., Ibata, R. A., Chapman, S. C., et al. 2008, AJ, 136, 1147
Belokurov, V., Zucker, D. B., Evans, N. W., et al. 2007, ApJ, 654, 897
Bertin, E., & Arnouts, S. 1996, A&AS, 117, 393
Bonnivard, V., Combet, C., Daniel, M., et al. 2015, MNRAS, 453, 849
Bovy, J. 2015, ApJS, 216, 29
Brown, T. M., Tumlinson, J., Geha, M., et al. 2014, ApJ, 796, 91
Caldwell, N., Walker, M. G., Mateo, M., et al. 2017, ApJ, 839, 20
Cantu, S. A., Pace, A. B., Marshall, J., et al. 2021, ApJ, 916, 81
Carlin, J. L., & Sand, D. J. 2018, ApJ, 865, 7
Carretta, E., Bragaglia, A., Gratton, R., D'Orazi, V., & Lucatello, S. 2009, A&A, 508, 695
Carrera, R., Pancino, E., Gallart, C., & del Pino, A. 2013, MNRAS, 434, 1681
Cerny, W., Pace, A. B., Drlica-Wagner, A., et al. 2021, ApJ, 910, 18
Cerny, W., Simon, J. D., Li, T. S., et al. 2022, arXiv:2203.11788
Chiti, A., Frebel, A., Ji, A. P., et al. 2018, ApJ, 857, 74
Chiti, A., Frebel, A., Ji, A. P., et al. 2022, arXiv:2205.01740
Chiti, A., Frebel, A., Simon, J. D., et al. 2021b, NatAs, 5, 392
Chiti, A., Mardini, M. K., Frebel, A., & Daniel, T. 2021a, ApJL, 911, L23
Choi, J., Dotter, A., Conroy, C., et al. 2016, ApJ, 823, 102
Chubak, C., Marcy, G., Fischer, D. A., et al. 2012, arXiv:1207.6212
Collins, M. L. M., Tollerud, E. J., Sand, D. J., et al. 2017, MNRAS, 467, 573
Cooper, M. C., Newman, J. A., Davis, M., Finkbeiner, D. P., & Gerke, B. F. 2012, spec2d: DEEP2 DEIMOS Spectral Pipeline, ascl:1203.003
Crnojevic, D., Sand, D. J., Zaritsky, D., et al. 2016, ApJL, 824, L14
de Jong, J. T. A., Harris, J., Coleman, M. G., et al. 2008, ApJ, 680, 1112
Dotter, A. 2016, ApJS, 222, 8
Dotter, A., Chaboyer, B., Jevremovic, D., et al. 2008, ApJS, 178, 89
Dressler, A., Bigelow, B., Hare, T., et al. 2011, PASP, 123, 288
Dressler, A., Hare, T., Bigelow, B. C., & Osip, D. J. 2006, Proc. SPIE, 6269, 62690F
Drlica-Wagner, A., Bechtol, K., Allam, S., et al. 2016, ApJL, 833, L5
Drlica-Wagner, A., Bechtol, K., Rykoff, E. S., et al. 2015, ApJ, 813, 109
Fabrizio, M., Merle, T., Thevenin, F., et al. 2012, PASP, 124, 519
Flaugher, B., Diehl, H. T., Honscheid, K., et al. 2015, AJ, 150, 150
Foreman-Mackey, D., Farr, W., Sinha, M., et al. 2019, JOSS, 4, 1864
Foreman-Mackey, D., Hogg, D. W., Lang, D., & Goodman, J. 2013, PASP, 125, 306
Frebel, A., Simon, J. D., & Kirby, E. N. 2014, ApJ, 786, 74
Gaia Collaboration, Brown, A. G. A., Vallenari, A., et al. 2021, A&A, 649, A1
Gaia Collaboration, Prusti, T., de Bruijne, J. H. J., et al. 2016, A&A, 595, A1
Geringer-Sameth, A., Koushiappas, S. M., & Walker, M. 2015, ApJ, 801, 74
Homma, D., Chiba, M., Okamoto, S., et al. 2016, ApJ, 832, 21
Homma, D., Chiba, M., Okamoto, S., et al. 2018, PASJ, 70, S18
Jenkins, S. A., Li, T. S., Pace, A. B., et al. 2021, ApJ, 920, 92
Jerjen, H., Conn, B., Kim, D., & Schirmer, M. 2018, arXiv:1809.02259
Ji, A. P., Frebel, A., Simon, J. D., & Geha, M. 2016, ApJ, 817, 41
Ji, A. P., Koposov, S. E., Li, T. S., et al. 2021, ApJ, 921, 32
Ji, A. P., Simon, J. D., Frebel, A., Venn, K. A., & Hansen, T. T. 2019, ApJ, 870, 83
Kallivayalil, N., Sales, L. V., Zivick, P., et al. 2018, ApJ, 867, 19
Kim, D., & Jerjen, H. 2015, ApJL, 808, L39
Kim, D., Jerjen, H., Geha, M., et al. 2016, ApJ, 833, 16
Kim, D., Jerjen, H., Mackey, D., Costa, G. S. D., & Milone, A. P. 2015, ApJL, 804, L44
Kim, S. Y., Peter, A. H. G., & Hargis, J. R. 2018, PhRvL, 121, 211302
Kirby, E. N., Boylan-Kolchin, M., Cohen, J. G., et al. 2013a, ApJ, 770, 16
Kirby, E. N., Cohen, J. G., Guhathakurta, P., et al. 2013b, ApJ, 779, 102

Kirby, E. N., Cohen, J. G., Simon, J. D., et al. 2017, ApJ, 838, 83
Kirby, E. N., Simon, J. D., & Cohen, J. G. 2015, ApJ, 810, 56
Koch, A., Wilkinson, M. I., Kleyna, J. T., et al. 2009, ApJ, 690, 453
Koposov, S. E., Belokurov, V., Torrealba, G., & Evans, N. W. 2015a, ApJ, 805, 130
Koposov, S. E., Casey, A. R., Belokurov, V., et al. 2015b, ApJ, 811, 62
Koposov, S. E., Walker, M. G., Belokurov, V., et al. 2018, MNRAS, 479, 5343
Laevens, B. P. M., Martin, N. F., Ibata, R. A., et al. 2015a, ApJL, 802, L18
Laevens, B. P. M., Martin, N. F., Bernard, E. J., et al. 2015b, ApJ, 813, 44
Li, T. S., Simon, J. D., Drlica-Wagner, A., et al. 2017, ApJ, 838, 8
Li, T. S., Simon, J. D., Kuehn, K., et al. 2018a, ApJ, 866, 22
Li, T. S., Simon, J. D., Pace, A. B., et al. 2018b, ApJ, 857, 145
Longeard, N., Martin, N., Ibata, R. A., et al. 2021, MNRAS, 503, 2754
Longeard, N., Martin, N., Starkenburg, E., et al. 2018, MNRAS, 480, 2609
Majewski, S. R., Skrutskie, M. F., Weinberg, M. D., & Ostheimer, J. C. 2003, ApJ, 599, 1082
Mateo, M., Olszewski, E. W., & Walker, M. G. 2008, ApJ, 675, 201
Mau, S., Cerny, W., Pace, A. B., et al. 2020, ApJ, 890, 136
Mau, S., Nadler, E. O., Wechsler, R. H., et al. 2022, ApJ, 932, 128
McConnachie, A. W., & Venn, K. A. 2020, AJ, 160, 124
McLaughlin, D. E., & van der Marel, R. P. 2005, ApJS, 161, 304
Minor, Q. E., Pace, A. B., Marshall, J. L., & Strigari, L. E. 2019, MNRAS, 487, 2961
Morganson, E., Gruendl, R. A., Menanteau, F., et al. 2018, PASP, 130, 074501
Munoz, R. R., Cote, P., Santana, F. A., et al. 2018, ApJ, 860, 66
Mucciarelli, A., Bellazzini, M., Ibata, R., et al. 2017, A&A, 605, A46
Mutlu-Pakdil, B., Sand, D. J., Carlin, J. L., et al. 2018, ApJ, 863, 25
Mutlu-Pakdil, B., Sand, D. J., Crnojevic, D., et al. 2021, ApJ, 918, 88
Nadler, E. O., Drlica-Wagner, A., Bechtol, K., et al. 2021, PhRvL, 126, 091101
Newman, J. A., Cooper, M. C., Davis, M., et al. 2013, ApJS, 208, 5
Oemler, A., Clardy, K., Kelson, D., Walth, G., & Villanueva, E. 2017, COSMOS: Observatories System for MultiObject Spectroscopy, ascl:1705.001
Okamoto, S., Arimoto, N., Yamada, Y., & Onodera, M. 2008, A&A, 487, 103
Pace, A. B., Erkal, D., & Li, T. S. 2022, arXiv:2205.05699
Pace, A. B., & Strigari, L. E. 2019, MNRAS, 482, 3480
Paxton, B., Bildsten, L., Dotter, A., et al. 2011, ApJS, 192, 3
Paxton, B., Cantiello, M., Arras, P., et al. 2013, ApJS, 208, 4
Paxton, B., Marchant, P., Schwab, J., et al. 2015, ApJS, 220, 15
Paxton, B., Schwab, J., Bauer, E. B., et al. 2018, ApJS, 234, 34
Rey, M. P., Pontzen, A., Agertz, O., et al. 2019, ApJL, 886, L3
Simon, J. D. 2019, ARA&A, 57, 375
Simon, J. D., & Geha, M. 2007, ApJ, 670, 313
Simon, J. D., Geha, M., Minor, Q. E., et al. 2011, ApJ, 733, 46
Simon, J. D., Drlica-Wagner, A., Li, T. S., et al. 2015, ApJ, 808, 95
Simon, J. D., Li, T. S., Drlica-Wagner, A., et al. 2017, ApJ, 838, 11
Simon, J. D., Li, T. S., Erkal, D., et al. 2020, ApJ, 892, 137
Spencer, M. E., Mateo, M., Walker, M. G., et al. 2017, AJ, 153, 254
Tarumi, Y., Yoshida, N., & Frebel, A. 2021, ApJL, 914, L10
Torrealba, G., Belokurov, V., Koposov, S. E., et al. 2018, MNRAS, 475, 5085
Torrealba, G., Koposov, S. E., Belokurov, V., et al. 2016b, MNRAS, 463, 712
Torrealba, G., Koposov, S. E., Belokurov, V., & Irwin, M. 2016a, MNRAS, 459, 2370
Walker, M. G., Mateo, M., & Olszewski, E. W. 2009a, AJ, 137, 3100
Walker, M. G., Mateo, M., Olszewski, E. W., et al. 2009b, ApJ, 704, 1274
Walker, M. G., Mateo, M., Olszewski, E. W., et al. 2016, ApJ, 819, 53
Walsh, S. M., Jerjen, H., & Willman, B. 2007, ApJL, 662, L83
Wenger, M., Ochsenbein, F., Egret, D., et al. 2000, A&AS, 143, 9
Willman, B. 2010, AdAst, 2010, 285454
Willman, B., Blanton, M. R., West, A. A., et al. 2005a, AJ, 129, 2692
Willman, B., Geha, M., Strader, J., et al. 2011, AJ, 142, 128
Willman, B., Dalcanton, J. J., Martinez-Delgado, D., et al. 2005b, ApJL, 626, L85
Willman, B., & Strader, J. 2012, AJ, 144, 76
Wolf, J., Martinez, G. D., Bullock, J. S., et al. 2010, MNRAS, 406, 1220
Youakim, K., Starkenburg, E., Martin, N. F., et al. 2020, MNRAS, 492, 4986
Zoutendijk, S. L., Júlio, M. P., Brinchmann, J., et al. 2021, arXiv:2112.09374
Zucker, D. B., Belokurov, V., Evans, N. W., et al. 2006, ApJL, 650, L41